Nanoscale

ROYAL SOCIETY OF CHEMISTRY

PAPER

View Article Online
View Journal

Cite this: DOI: 10.1039/d5nr03101j

Spectroscopic investigation of the influence of Ni particle size in CO_2 methanation

Majed Alam Abir, [a] Mihir Kulkarni, [b] Rachel E. Phillips,[a] Joseph Z. M. Harrah[a] and Madelyn R. Ball *[a,b]

Received 22nd July 2025,
Accepted 11th December 2025

DOI: 10.1039/d5nr03101j

rsc.li/nanoscale

CO_2 methanation was investigated over Ni/Al_2O_3 catalysts with Ni nanoparticle sizes ranging from 4.6 to 8.4 nm. Particle sizes were determined using electron microscopy and CO chemisorption measurements. The turnover frequency (TOF) increased from 0.005 s^{-1} to 0.21 s^{-1} with increasing Ni particle size. To understand the origin of this trend, *in situ* FTIR studies were performed. The results revealed that smaller Ni particles predominantly followed a direct formate pathway, while larger particles exhibited a combined CO and formate-mediated mechanism. Although surface basicity varied among the catalysts, methanation activity was not correlated with this basicity. However, the ability of the catalysts to undergo reduction and oxidation was suggested to cooperatively enhance methanation activity.

Introduction

The increasing concentration of atmospheric carbon dioxide (CO_2), primarily from anthropogenic activities, poses a significant global challenge, motivating the development of effective strategies for its capture and utilization.[1,2] Among various approaches for CO_2 utilization, methanation ($CO_2 + 4H_2 \rightleftharpoons CH_4 + 2H_2O$) has emerged as a promising technology.[2,3] This reaction offers two simultaneous benefits: it is a route to transform a greenhouse gas into a valuable energy carrier (CH_4, synthetic natural gas), and it provides a pathway for storing renewable hydrogen, thus contributing to a circular carbon economy.[4,5]

The development of efficient catalysts is key to enabling CO_2 methanation.[2] Heterogeneous catalysts such as Ni-based catalysts offer a balance of high activity, high methane selectivity, and low cost, making them economically attractive for large-scale applications.[6,7] The performance of Ni-based catalysts is highly influenced by several factors, including metal loading, the size of the dispersed Ni nanoparticles, metal–support interactions (MSI), and the properties of the support material.[8–14]

The size of Ni nanoparticles significantly influences both the reactivity and stability in CO_2 methanation, as particle size affects the electronic and geometric properties of the catalyst.[15,16] The structure sensitivity of supported Ni catalysts in methanation has been explored using a combination of experimental and computational methods.[10,17] Wang *et al.* studied 3.5–7.5 nm Ni particles on SiO_2 support and found that the catalyst with the smallest Ni particles had the highest methanation reactivity.[18] Similarly, Vogt *et al.* demonstrated that the catalytic mechanism of CO_2 reduction is affected by Ni nanoparticle size (1–7 nm) on a SiO_2 support where they found a volcano trend of methanation activity with Ni particle size and the highest TOF for the catalysts with ~4 nm Ni particles. Catalysts exhibited higher activity when the coverage of linearly adsorbed CO is higher.[10] Complementarily, Sterk *et al.* employed density functional theory (DFT) and microkinetic modeling to reveal how CO_2 methanation activity varies across different Ni crystal facets.[19] Using density functional theory (DFT) and microkinetic modeling, they found that the terrace surfaces Ni(111) and Ni(100), as well as the stepped Ni(211) facet, exhibited minimal activity for CO_2 methanation. In contrast, the Ni(110) surface was identified as the most active. Their analysis revealed that the dominant reaction mechanism involves a combination of carbide and formate pathways. Spanò *et al.* used DFT calculations to study a broad range of Ni metal nanoparticles with different shapes and sizes in the range of 0.5–10 nm in CO_2 methanation, quantifying the distribution of potential active sites for each particle.[20] They found a maximum turnover frequency (TOF) for nanoparticles around 2–3 nm and, importantly, that the particle shape impacts the structure sensitivity. These studies demonstrated structure sensitivity by considering nickel as the sole active site, without considering the potential catalytic contributions of the support.

However, supports such as Al_2O_3,[21] CeO_2,[22] TiO_2,[23] and ZrO_2[24] can actively participate in CO_2 methanation to improve catalytic activity, indicating that structure sensitivity involving

---

[a] *Department of Chemical and Biomedical Engineering, West Virginia University, Morgantown, WV 26506, USA*
[b] *Department of Chemical Engineering and Materials Science, Michigan State University, East Lansing, MI 48824, USA. E-mail: mball@msu.edu*

active supports should also be explored for the rational design of more efficient methanation catalysts. Lin *et al.* investigated structure sensitivity experimentally by studying partially reducible CeO_2-supported catalysts with Ni particle sizes of 2, 4, and 8 nm for CO_2 methanation.[25] Their findings showed that the methanation activity increases with Ni particle size. Moreover, it was found from DRIFTS experiments that the hydrogenation of surface formate species was markedly more efficient on the larger (8 nm) Ni particles supported on CeO_2 compared to smaller particles. Adhikari *et al.* experimentally studied CO_2 methanation over Ni/CeO_2 catalysts with Ni particle sizes ranging from 1.3 to 17 nm. While CeO_2 was found to enhance Ni reducibility, its acid–base and redox properties had minimal influence on the methanation activity. Notably, methane selectivity increased with larger Ni particle sizes.[26] In our previous work, we examined Ni particle sizes ranging from 7.7 to 62.5 nm on a reducible CeO_2 support and from 2.9 to 27 nm on a reducible TiO_2 support for CO_2 methanation.[27] We demonstrated a connection between the size of Ni particles, their corresponding adsorbed surface species, and their reactivity for CO_2 methanation.

Another promising support for nickel-based CO_2 methanation is alumina (Al_2O_3).[28,29] Al_2O_3 is active[30,31] but not reducible, therefore it has different behavior and interaction with metal nanoparticles than TiO_2 or CeO_2. While numerous studies have focused on the reaction mechanism, Ni loading, addition of a second metal or a second support, the role of the alumina support, and the interaction between nickel and alumina in CO_2 methanation, structure sensitivity has not been extensively detailed in the literature for Al_2O_3 supported Ni catalysts.[32–36] Zhang *et al.* investigated CO_2 methanation over Ni/Al_2O_3 catalysts by varying the Ni loading from 2.5 to 50 wt%, which led to Ni particle sizes between 11.6 and 17.8 nm.[37] Their study revealed that with different nickel loadings, nickel particle agglomeration was influenced by the varied strength of interaction between metal and alumina. Among the samples, the catalyst with approximately 25 wt% Ni (12 nm Ni particles) exhibited the highest methanation activity. Additionally, Karelovic *et al.* examined the effect of Rh particle size on Al_2O_3-supported catalysts, with sizes ranging from 3.6 to 15.4 nm.[38] Their study showed that the intrinsic activity of Rh/Al_2O_3 catalysts for CO_2 methanation was largely independent of particle size at reaction temperatures between 185 and 200 °C. However, at lower temperatures, catalysts with larger Rh particles exhibited higher activity.

In this work, we investigate the structure sensitivity of Al_2O_3-supported Ni catalysts for CO_2 methanation. To obtain the range of Ni particle sizes, the catalysts were synthesized using strong electrostatic adsorption (SEA), colloidal synthesis (CS), and incipient wetness impregnation (IWI) methods. Comprehensive characterization techniques—including CO chemisorption, temperature-programmed reduction (TPR), temperature-programmed oxidation (TPO), (scanning) transmission electron microscopy (STEM/TEM), and CO_2 temperature-programmed desorption (TPD) were employed to investigate the structural properties of the catalysts. Reactivity measurements were performed in a fixed-bed flow reactor to establish correlations between the catalyst structure and CO_2 methanation performance. *In situ* diffuse reflectance infrared Fourier transform spectroscopy (DRIFTS) was applied to investigate how the reaction mechanism is influenced by variations in Ni particle size on an Al_2O_3 support. Our results demonstrate that changes in Ni particle size on an Al_2O_3 support influence the reaction mechanism and reduction behavior, which in turn account for the observed trends in CO_2 methanation performance.

Materials and methods

Catalyst synthesis

Alumina supported Ni catalysts were synthesized with varied particle sizes by three different methods. The support oxide, fumed Al_2O_3 (AEROXIDE® Alu 130, Evonik) was used as received. This alumina exists in the γ-phase confirmed by XRD (Fig. S1). All catalysts are referred to as Ni/Al_2O_3-*X*, where *X* is the particle size measured by electron microscopy.

Strong electrostatic adsorption. Supported Ni catalysts were prepared by strong electrostatic adsorption (SEA).[39–41] The catalysts have a theoretical Ni loading of between 3 and 10 wt%. The desired amount of hexamine nickel(II) chloride (Strem Chemicals, 98%) was dissolved in 75 mL of deionized water (18 MΩ) to synthesize 5 g catalyst in each batch. The pH of the solution was then adjusted to 12 *via* dropwise addition of an ammonium hydroxide solution (Sigma-Aldrich, 30%). Once the solution had a stable pH of 12, the oxide support was added and stirred for one hour. After mixing, the catalyst solution was filtered and washed with 1.5 L of deionized water and left to dry at room temperature in air overnight. The catalyst was then transferred to a ceramic crucible and dried in static air at 120 °C for 30 minutes. The dry catalyst was crushed into a fine powder and then reduced in flowing H_2 (50 sccm) (Airgas, Industrial). The catalyst was first heated to 227 °C and held for 2 hours, then heated to 477 °C and held for 12 hours (all heating at 2 °C per minute).[42] Then, the catalyst was cooled under H_2 to below 40 °C, purged with N_2 (Airgas, Industrial), then passivated with 10.02% O_2 in Ar (Airgas, Ultra High Purity) at 10 sccm for 30 minutes.

Incipient wetness impregnation. To synthesize a Ni/Al_2O_3 catalyst with larger Ni nanoparticles, we used incipient wetness impregnation (IWI).[43] First, the wetness point of the support was measured and determined to be 0.848 g of deionized water per g of Al_2O_3. The catalysts have a theoretical Ni loading of between 3 and 15 wt%. The desired amount of hexamine nickel(II) chloride (Strem Chemicals, 98%) was dissolved in deionized water (18 MΩ) according to the Al_2O_3 wetness point to synthesize 5 g catalyst. The metal solution was added dropwise to the Al_2O_3 support, mixing well between each addition. The catalyst was then transferred to a ceramic crucible and dried in static air at 120 °C for 30 minutes. The dry catalyst was crushed into a fine powder and then reduced in flowing H_2 (50 sccm) (Airgas, Industrial). The catalyst was heated to 227 °C and held for 2 hours, then heated to 477 °C and held for 12 hours (all heating at 2 °C per minute).[42] Then, the catalyst was cooled under H_2 to below 40 °C, purged with N_2 (Airgas, Industrial), then passivated with 10.02% O_2 in Ar (Airgas, Industrial) at 10 sccm for 30 minutes.

Colloidal synthesis. To synthesize a Ni/Al_2O_3 catalyst with particularly small Ni nanoparticles, we used colloidal synthesis (CS). Colloidal Ni nanoparticles were synthesized using a procedure adapted from Vrijburg *et al.*[44] First, nickel acetylacetonate hydrate (Strem Chemicals) (2.57 g), oleylamine (Sigma-Aldrich, 70%) (150 mL), and oleic acid (Sigma-Aldrich, 90%) (3.2 mL) were added to a 250 mL round bottom flask. This solution was degassed under bubbling Ar (Airgas, Industrial) for 30 minutes at 110 °C, then cooled to 90 °C. In parallel, a solution of borane *tert*-butylamine (BTB) (Thermo Scientific, 97%) (4.4 g) and oleylamine (20 mL) were mixed in a 50 mL flask and degassed under Ar at room temperature for 30 minutes. Then, the BTB solution was added to the Ni acetylacetonate solution within a 10 second period while maintaining an Ar atmosphere and constant stirring. Within 30 seconds of the addition, the solution turned from light blue to dark grey or black. The mixture was stirred at 90 °C for 1 hour. Next, toluene (Sigma-Aldrich, 99.8%) (170 mL) was added to the mixture to precipitate the nanoparticles, and the mixture was cooled to room temperature. The solution was separated into centrifuge tubes, each with ∼15 mL of the nanoparticle solution and then ∼35 mL of acetone (VWR Chemicals) was added. The solution was centrifuged at 10 000 rpm for 10 minutes then the supernatant was removed. Additional acetone was added to each tube and sonicated to redisperse the nanoparticles; this washing process was repeated three more times. From here, the washed nanoparticles were sonicated once more in acetone to disperse the nanoparticles. Then, the Al_2O_3 support was impregnated with the nanoparticle solution to achieve the desired metal loading (3 wt%) to synthesize 5 g total catalyst. After sufficient solution was added to reach the wetness point of the Al_2O_3 support, the mixture was placed in a drying oven at 120 °C for 30–40 minutes or until the acetone had evaporated. Then, additional nanoparticle solution was added, and the process was repeated until the desired Ni loading was achieved, based on the total Ni content and assuming uniform distribution of nanoparticles in the solution. The dried catalysts were reduced in H_2 (50 sccm) at 350 °C (heating rate of 2 °C min^{-1}) for 5 hours. The catalyst was cooled to below 40 °C, purged with N_2, and passivated with 10.02% O_2 in Ar (Airgas, Industrial) at 10 sccm for 30 minutes.

Reactivity measurements

CO_2 methanation reactions were carried out in a 0.375-in. outer diameter and 0.340-in. inner diameter stainless-steel flow reactor. 270–300 mg of catalyst for Ni/Al_2O_3-4.6, Ni/Al_2O_3-5.6, and Ni/Al_2O_3-6.6; 100 mg of catalyst for Ni/Al_2O_3-7.4; and 26 mg of catalyst for Ni/Al_2O_3-8.4 were diluted in silicon carbide (Strem Chemicals, 100 mesh) at a mass ratio of 1 : 3 catalyst to silicon carbide. The diluted catalyst was loaded into the reactor between plugs of quartz wool (Technical Glass Products). The temperature was controlled using a proportional-integral-derivative (PID) controller (Love Controls) with a K-type thermocouple (Omega) placed inside the catalyst bed. Aluminum blocks were placed between the reactor tube and the furnace (Applied Test Systems) to ensure isothermal operation. All gases were delivered by mass flow controller (Brooks 5850 (CO_2, H_2) and Alicat (N_2)) and used without further purification. Prior to reaction, the catalyst was reduced under H_2 (Airgas, Industrial) flow for 2 hours at 477 °C (50 sccm) (heating at 5 °C min^{-1}). The reactor was cooled to 300 °C with a ramp rate of 17 °C min^{-1} under H_2 then a mixture of CO_2 (Airgas, Bone-Dry), H_2, and N_2 (Airgas, Industrial) was fed to the reactor at a molar ratio of 1 : 4 : 5. Reactions were conducted for a minimum of 20 hours. Gas composition was measured *via* gas chromatograph (PerkinElmer Clarus® 580 GC) with Ar carrier gas and a thermal conductivity detector (TCD) with Haysep N and mole sieve 13× columns and a flame ionization detector (FID) with an Elite-Q Plot column. N_2 was used as an internal standard. All measurements were carried out at a CO_2 conversion of less than 10% and the carbon balance for all reactions was >98%. The average CO_2 conversion and reactivity data were taken after an activation period and with a standard deviation of not more than 0.3% (X% ± 0.3%, here X is the CO_2 conversion) for 5 hours (Table 2). The absence of transport limitations were confirmed in this study (Tables S1 and S2).

In a similar manner, CO hydrogenation was conducted in the same differential reactor as described for CO_2 methanation. 100 mg of catalyst was diluted in silicon carbide (Strem Chemicals, 100 mesh) at a mass ratio of 1 : 3 catalyst to silicon carbide. The diluted catalyst was loaded into the reactor between plugs of quartz wool (Technical Glass Products). Prior to reaction, the catalyst was reduced under H_2 (Airgas, Industrial) flow for 2 hours at 477 °C (50 sccm) (heating at 5 °C min^{-1}). The reactor was cooled to 300 °C with a ramp rate of 17 °C min^{-1} under H_2 then a mixture of 10% CO/Ar (Airgas, UHP), H_2, and N_2 (Airgas, Industrial) was fed to the reactor at a molar ratio of 1 : 4 : 5. Reactions were conducted for 3 hours.

Characterization

Chemisorption, temperature programmed reduction, temperature programmed oxidation, and temperature programmed desorption experiments were all conducted on a Micromeritics Flex. The Ni dispersion was evaluated by static CO chemisorption at 35 °C. For chemisorption, catalysts were pre-reduced in H_2 (Airgas, UHP) at 477 °C for 2 h. with a ramp rate of 10 °C min^{-1}. CO was incrementally dosed up to a pressure of 450 mmHg. The site density was calculated using a stoichiometry calculating from the linear and bridged CO adsorption area from CO FTIR, described in more detail in the main text.

For temperature programmed reduction (TPR) experiments, the catalysts were first dried under N_2 (50 sccm) at 110 °C for 30 minutes (ramp rate 10 °C min^{-1}), then cooled to 40 °C. TPR was run while flowing 10% H_2/Ar (Matheson) at 50 sccm and heating at 10 °C min^{-1} up to 950 °C and the gas composition was monitored by TCD.

Similarly, for temperature programmed oxidation (TPO) experiments, the catalysts were first dried under N_2 (50 sccm) at 110 °C for 30 minutes (ramp rate 10 °C min^{-1}), then cooled to 40 °C. TPO was run while flowing 10% O_2/He (Airgas) at 50 sccm and heating at 10 °C min^{-1} up to 950 °C and the gas composition was monitored by TCD.

For temperature programmed desorption (TPD) of CO_2, the catalyst was first reduced in H_2 (Airgas, UHP) to 477 °C for 2 h with a ramp rate of 10 °C min^{-1}. Then the sample was cooled to 100 °C and purged under flowing He (Matheson, UHP) for 30 minutes. The sample was then exposed to 10% CO_2/Ar (Matheson) at 25 sccm for 90 minutes and desorption conducted by heating to 900 °C at 10 °C min^{-1}.

Transmission electron microscopy (TEM) was carried out on a JEOL TEM 2100. For the unsupported colloidal nanoparticles, one drop of the Ni nanoparticle solution was placed onto a 300-mesh copper grid with a carbon-coated formvar film and then air-dried. Images were acquired at 120 kV with a Gatan OneView camera and Digital Micrograph software. Scanning transmission electron microscopy (STEM) was carried out on a JEOL NEOARM aberration-corrected analytical STEM at Oak Ridge National Laboratory (ORNL) operated at 200 kV with a semi-convergence angle of ~28 mrad for capturing images on supported catalysts. The supported catalysts were dispersed in acetone and then a copper grid (400-mesh with a carbon-coated formvar film) was dipped into this solution once and air-dried. Particle size analysis was conducted using ImageJ.

Fourier transform infrared spectroscopy (FTIR) experiments were conducted using a Nicolet iS50 FTIR (Thermo-Fisher) with a mercury–cadmium–telluride (MCT) detector. Samples were loaded in a high temperature diffuse reflection cell (Harrick Praying Mantis) equipped with CaF_2 windows. To investigate the catalyst behavior under CO_2 methanation conditions, all catalysts were first reduced under a mixture of H_2 and Ar (1 : 9 ratio) at 74 sccm at 477 °C (heating at 5 °C min^{-1}) for 2 hours and then cooled to 300 °C with a ramp rate of 17 °C min^{-1} under the mixture of H_2 and Ar (1 : 9 ratio) prior to switching to a mixture of CO_2, H_2, and Ar (1 : 4 : 5 ratio) at 100 sccm in the IR cell. For transient experiments, CO_2 was stopped by switching the gas to a mixture of H_2 and Ar (4 : 5 ratio) at 90 sccm and maintaining this flow for 1 h. CO_2 flow was then restarted, switching to a mixture of CO_2, H_2, and Ar (1 : 4 : 5 ratio) at 100 sccm and maintaining flow for 30 minutes. Similarly, CO hydrogenation *in situ* FTIR experiments were conducted by reducing the catalysts first as mentioned above and then cooling to 300 °C. Then the catalysts were exposed to a mixture of CO, H_2, and Ar (7 : 31 : 62 ratio) at 100 sccm in the IR cell. All spectra include 8 accumulated scans at a resolution of 4 cm^{-1}. Similarly, for CO adsorption FTIR experiments, all catalysts were first reduced under a mixture of H_2 and Ar (1 : 9 ratio) at 74 sccm at 477 °C (heating at 5 °C min^{-1}) for 2 hours. After reduction, the sample was cooled to 35 °C with a ramp rate of 17 °C min^{-1} under Ar flow at 60 sccm. The flow was then switched to a mixture of CO and Ar (1 : 9) ratio at 20 sccm in the IR cell for 1 hour and finally switched to only Ar at 60 sccm. All spectra include 256 accumulated scans at a resolution of 4 cm^{-1}.

Inductively coupled plasma optical emission spectroscopy (ICP-OES) was conducted on an Agilent ICP OES 720 instrument, following EPA 200.7 Rev 4.4–1994 Method for Ni. ICP samples were prepared by dissolving 25 mg of catalyst in 10 mL aqua regia ($HCl : HNO_3 = 3 : 1$) for at least 24 hours at room temperature.

X-ray diffraction (XRD) patterns were measured on an X'Pert PRO MRD instrument (PANalytical) with Cu Kα (l = 1.5056 Å) radiation with a 2θ scan step size of 0.016.

X-ray photoelectron spectra (XPS) were collected on fresh and spent Ni/Al_2O_3-4.6 and Ni/Al_2O_3-8.4 catalysts using a Kratos Axis Supra + X-ray Photoelectron Spectroscope equipped with a monochromatic Al Kα (1486.7 eV) X-ray source. The survey scans were performed at a pass energy of 160 eV and step size of 1 eV, while the individual scans at 20 eV with a step size of 0.1 eV. The spectra were processed and fit in CasaXPS software[45] with a Shirley-type background, and a spectrum shift calibration was performed using C 1s peak at 284.8 eV.

Results and discussion

Nickel catalysts supported on alumina were synthesized using colloidal synthesis (CS), strong electrostatic adsorption (SEA), and incipient wetness impregnation (IWI) methods. Table 1 summarizes the set of catalyst samples, including Ni loading, metal dispersion, particle size determined from CO chemisorption measurements, and STEM/TEM.

We compared the estimated Ni nanoparticle size measured from CO chemisorption and STEM/TEM. To estimate active sites from chemisorption, if we use a stoichiometry of 1.5 Ni : CO, assuming a mix of atop and bridge bound CO, the particle size estimated from CO chemisorption does not agree well with (S)TEM (Table S3). From CO FTIR on Ni/Al_2O_3-8.4, however, we can better estimate the CO adsorption behavior on these catalysts by taking into account the relative quantities of linear and bridged CO adsorption. As shown in Fig. S2, the peak area for the bridge bound CO (1740–2000 cm^{-1}) is almost 3 times larger than the peak area for linearly adsorbed CO (2000–2100 cm^{-1}).[46,47] While exact extinction coefficients are not measured, we estimate the CO adsorption stoichiometry to be around 1.3 based on generally reported ratios of linear and bridged CO molar extinction coefficients on a variety of different metals (Table S4).[48–50] This estimate and the corresponding IR spectra suggests that CO adsorption on our catalysts does not follow the typical approximation of a Ni : CO stoichiometry of 1.5.[51] Due to the uncertainty in this adsorption stoichiometry, however, we have applied the sites estimated using the Ni particle size measured from STEM/TEM (Fig. 1) for all subsequent discussion. For the catalyst prepared *via* colloidal synthesis (CS), the initially synthesized unsupported Ni nanoparticles exhibited an average diameter of 3.16 ± 0.69 nm (Fig. S3). Upon incorporation onto the Al_2O_3

Table 1 Metal loading, synthesis conditions, and particle size and site density measured by CO chemisorption and electron microscopy for the Ni/Al_2O_3 catalysts studied in this work

Catalyst name[a]	Synthesis method[b]	Theoretical Ni wt (%)	ICP Ni wt (%)	Reduction temp. (°C)	Site density (μmol g^{-1}) from CO chemi[c]	Particle size (nm) from CO chemi[d]	Particle size[e] (nm)	Site density (μmol g^{-1}) from STEM/TEM[f]
Ni/Al_2O_3-4.6	CS	3	2.23	350	121.6	3.2	4.6 ± 1.4	82.6 ± 25.1
Ni/Al_2O_3-5.6	SEA	3	2.3	477	68.7	5.7	5.6 ± 1.3	70 ± 16.2
Ni/Al_2O_3-6.6	IWI	3	2.3	477	60.5	6.5	6.6 ± 1.3	59.4 ± 11.7
Ni/Al_2O_3-7.4	SEA	10	6.66	477	150.1	7.6	7.4 ± 1.5	153.3 ± 31.1
Ni/Al_2O_3-8.4	IWI	15	14.7	477	315.1	7.9	8.4 ± 1.9	298.1 ± 67.4

[a] Catalysts are named as Ni/Al_2O_3-X where X is the Ni particle size in nm measured from STEM/TEM. [b] CS: colloidal synthesis, SEA: strong electrostatic adsorption, IWI: incipient wetness impregnation. [c] Site density was calculated from CO static chemisorption based on ICP weight percentage and using a stoichiometry calculated from CO FTIR as described in Fig. S2. [d] Ni particle size was calculated using the formula, $d_{Ni} = 1.0/D$ where D is the dispersion calculated from CO static chemisorption.[29] [e] Average particle size and standard deviation measured from TEM (6.6 and 8.4 nm samples) or STEM (4.6, 5.6, and 7.4 nm samples) (Fig. 1) considering 65 nanoparticles for each sample. [f] Site density was calculated from the STEM/TEM particle size and weight loading determined from ICP.

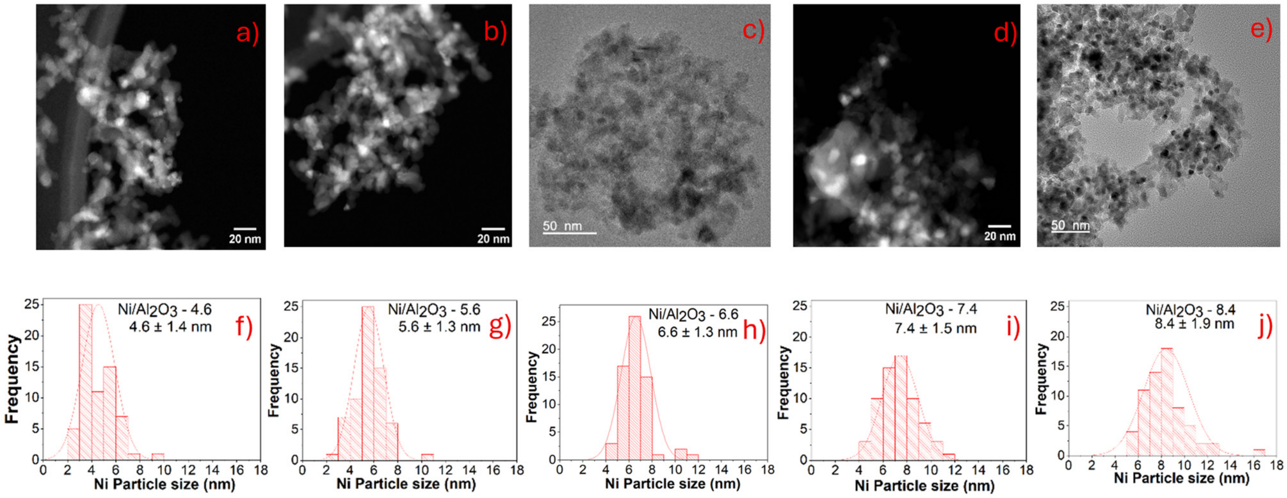

Fig. 1 STEM/TEM images for (a) Ni/Al_2O_3-4.6, (b) Ni/Al_2O_3-5.6, (c) Ni/Al_2O_3-6.6, (d) Ni/Al_2O_3-7.4, (e) Ni/Al_2O_3-8.4, and corresponding particle size distributions (f–j) for the catalysts studied in this work. For each sample, 65 nanoparticles were measured, and the Ni particle sizes are shown as mean ± standard deviation.

support, the Ni particle size was 3.2 nm from chemisorption, while STEM analysis revealed a size of 4.6 ± 1.4 nm. We note there is potential for some of the Ni to be in phases that do not adsorb CO, *e.g.*, nickel aluminate[31] which was confirmed from XRD (Fig. S1). We emphasize that comparing active site estimates from chemisorption with each stoichiometry and STEM analysis results in only minor variations in site density. These differences likely arise from a combination of factors, namely variations in the CO : Ni adsorption stoichiometry and relative proportion of Ni adsorption sites *vs.* aluminate non-adsorption sites across the set of samples. Despite the inherent uncertainty in estimating active site densities, the overall behavior of these catalysts as a function of particle size does not change substantially.

The CO_2 methanation reaction was carried out over the Ni/Al_2O_3 catalysts. The activity is reported in Table 2 and the corresponding time on stream data is shown in Fig. S4. Each reaction was conducted for a minimum of 20 hours. The Ni/Al_2O_3-4.6 and Ni/Al_2O_3-5.6 catalysts were stable from the beginning, whereas Ni/Al_2O_3-6.6, Ni/Al_2O_3-7.4, and Ni/Al_2O_3-8.4 showed an activation period for 5, 8, and 20 h., respectively, before reaching steady state (Fig. S4). The weight hourly space velocity (WHSV) ranged from 5000 to 280 000 h^{-1}, with CO_2 conversion maintained below 10%. The absence of transport limitations was verified, as shown in Table S2. The reported CO_2 conversion and CH_4 production rates were calculated from the steady state activity after the activation period. Methane production rates (μmol min^{-1} g^{-1} catalyst), shown in Table 2, were normalized by the corresponding electron microscopy-based site densities in Table 1, yielding the turnover frequencies (TOFs) presented in Table 2 and Fig. 2.

As shown in Fig. 2 and Fig. S5, we observed an increase in TOF with increasing Ni particle size for CO_2 methanation. Although slight differences in TOF values are observed between those calculated from CO chemisorption–derived and microscopy-based site densities, the overall trend of TOF with

Table 2 CO_2 methanation reactivity data of the set of Ni/Al_2O_3 catalysts

Catalyst	Total flow rate (sccm)	WHSV (1/hr)	Average CO_2 conversion[a] (%)	Average CH_4 Production (μmol min^{-1} g^{-1} of catalyst)[a]	TOF[b] (s^{-1})
Ni/Al_2O_3-4.6	56	5100	4.1 ± 0.2	22.5 ± 0.09	0.005 ± 0.001
Ni/Al_2O_3-5.6	100	8100	6.9 ± 0.1	82.4 ± 0.6	0.02 ± 0.005
Ni/Al_2O_3-6.6	200	17 500	8.7 ± 0.1	177 ± 1.3	0.05 ± 0.01
Ni/Al_2O_3-7.4	300	71 000	8.8 ± 0.1	829 ± 2.5	0.09 ± 0.02
Ni/Al_2O_3-8.4	300	28 400	9.4 ± 0.3	3757 ± 8	0.21 ± 0.05

[a] Average CO_2 conversion and corresponding rates were taken over 5 h. Time on stream when the standard deviation in conversion was 0.3% or less over time (Table S5). In this window, the standard deviation for the average CH_4 production was found to be 8 μmol min^{-1} g_{cat}^{-1} or less over time. Reaction conditions: $CO_2 : H_2 : N_2 = 1 : 4 : 5$, 300 °C and 1 atm. The catalysts were reduced for 2 h. at 477 °C prior to reaction. All the catalysts were 100% selective to CH_4. [b] TOF was calculated using the electron microscopy based site densities; error in TOF accounts for error in the CH_4 production and the standard deviation of the measured particle size from Table 1.

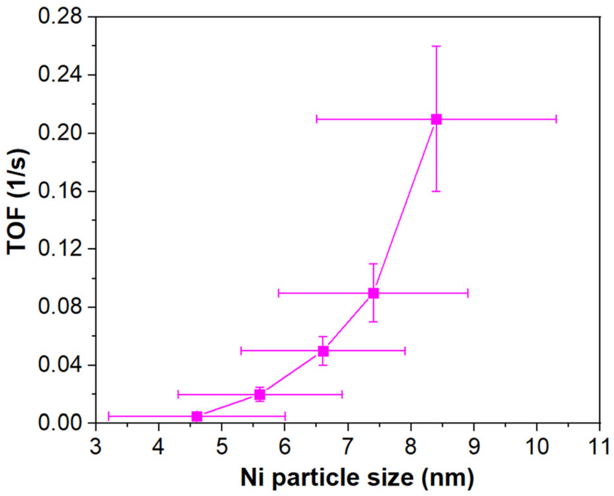

Fig. 2 Turnover frequency as a function of Ni particle size from (S)TEM for catalysts supported on Al_2O_3. The lines are to guide the eye. Reaction conditions: 300 °C, 1 atm, $CO_2 : H_2 : N_2 = 1 : 4 : 5$.

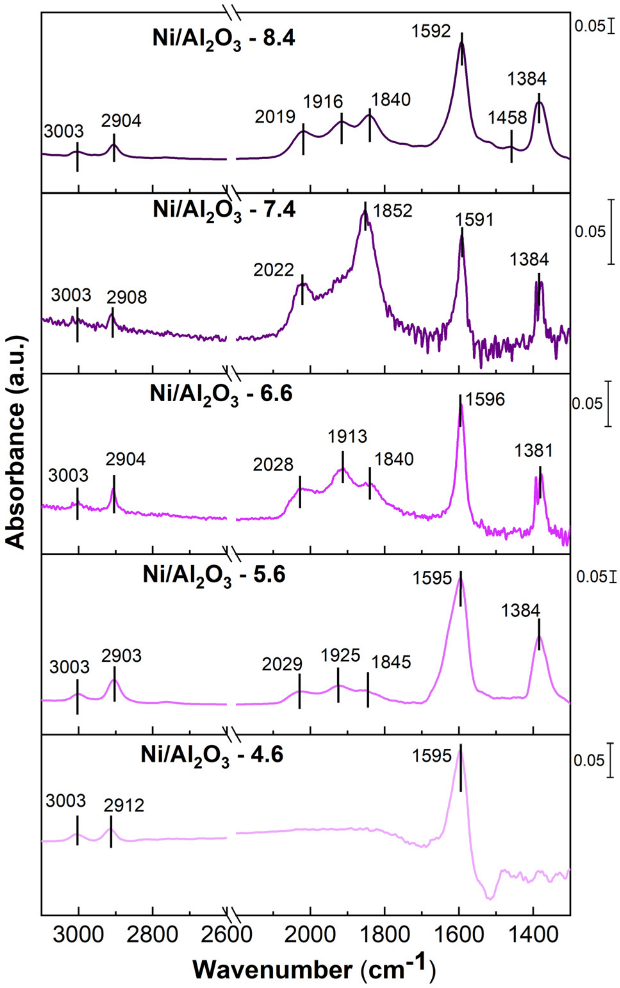

Fig. 3 FTIR spectra of Ni/Al_2O_3 catalysts under CO_2 methanation conditions. All catalysts were reduced *in situ* at 477 °C for 2 h prior to switching to the CO_2, H_2, Ar mixture at 300 °C. The spectra shown were collected after 10 h. of reaction and the background of the reduced catalysts under H_2/Ar flow is subtracted.

Ni particle size remains consistent as shown in Fig. S5. To understand the underlying reasons for this trend, we investigated the reaction mechanism using *in situ* FTIR spectroscopy. The results, presented in Fig. 3, provide insights into how the surface species under reaction conditions vary with Ni particle size. Detailed peak assignments are provided in Table S6a.

As shown in Fig. 3 and Table S6a, we observe peaks assigned to formate species on all catalysts: at 1595 and 2912 cm^{-1} for Ni/Al_2O_3-4.6, 1384, 1595, and 2903 cm^{-1} for Ni/Al_2O_3-5.6, 1381, 1596, and 2904 cm^{-1} for Ni/Al_2O_3-6.6, 1384, 1591, and 2908 cm^{-1} for Ni/Al_2O_3-7.4, and 1384, 1592, and 2904 cm^{-1} for Ni/Al_2O_3-8.4.[52–56] We also observed peaks corresponding to three-fold and bridge bound CO at 1840 and 1925 cm^{-1} for Ni/Al_2O_3-5.6, 1840 and 1913 cm^{-1} for Ni/Al_2O_3-6.6, 1852 cm^{-1} for Ni/Al_2O_3-7.4, and 1840 and 1916 cm^{-1} for Ni/Al_2O_3-8.4. Peaks assigned to linear CO are observed at 2029 cm^{-1} for Ni/Al_2O_3-5.6, 2028 cm^{-1} for Ni/Al_2O_3-6.6, 2022 cm^{-1} for Ni/Al_2O_3-7.4, and 2019 cm^{-1} for Ni/Al_2O_3-8.4.[52,53,57,58] Linear and bridged CO species were absent on the smallest Ni particle size catalyst (Ni/Al_2O_3-4.6). A peak at 3003 cm^{-1} was observed for all the catalysts and can be assigned to the asymmetric C–H stretching vibration of either adsorbed methane or formate.[52,53,57] We also observe a peak at

1458 cm^{-1} for Ni/Al$_2$O$_3$-8.4 (Fig. 3) which is assigned to a bicarbonate species[53,58,59] formed on the Ni-Al$_2$O$_3$ interface. While previous reports have suggested that surface carbonate and carboxylate species participate in the reaction mechanism, we did not observe these species on our catalysts.[60] On the smallest particles, we have observed only formate species. We also note that 1800–2100 cm^{-1} broadly corresponds to peaks for CO species adsorbed on metallic Ni,[61,62] while formate species typically adsorb and stabilize on NiO rather than on metallic Ni,[63,64] suggesting both Ni species are present under reaction conditions. As the Ni particle size increased, we also observed CO as well as bicarbonate for the catalyst with the largest particle size. These observations suggest a shift in the reaction mechanism with particle size.

To quantitatively compare the set of catalysts, we integrated the total peak areas for both carbonyl (2150–1800 cm^{-1}) and formate species (summation of peaks at 1384, 1591–1595, and 2903–2908 cm^{-1}) and calculated the ratio of carbonyl to formate peak areas as shown Fig. 5a. We observe that this ratio of carbonyl : formate is higher for Ni/Al$_2$O$_3$-7.4 than for Ni/Al$_2$O$_3$-5.6 and Ni/Al$_2$O$_3$-6.6. We suggest that this increase in coverage of carbonyl species is responsible for the higher activity of Ni/Al$_2$O$_3$-7.4 compared to Ni/Al$_2$O$_3$-5.6 and Ni/Al$_2$O$_3$-6.6. This difference in surface coverage for carbonyl and formate species, however, does not explain why Ni/Al$_2$O$_3$-8.4 has the highest activity as the ratio of carbonyl to formate peak areas was lower than for Ni/Al$_2$O$_3$-7.4. During the initial time on stream under reaction conditions (Fig. S6), a small peak corresponding to a formyl species[65] at 1742 cm^{-1} was observed for Ni/Al$_2$O$_3$-8.4, but then disappeared after 10 min. We suggest that both the formyl species and the interfacial bicarbonate species described above are highly active intermediates,[66–68] leading to the higher observed rate over the Ni/Al$_2$O$_3$-8.4 catalyst. We note that DRIFTS analysis by Rivero-Mendoza *et al.* revealed a similar presence of formate and adsorbed CO species on a La–Ni/Al$_2$O$_3$ catalyst surface. They suggested these adsorbed species correspond to a reaction pathway involving H$_2$-assisted CO$_2$ dissociation into C and O atoms, which are subsequently hydrogenated to form CH$_4$ and H$_2$O.[69]

To further probe the mechanism and role of adsorbed species, we then stopped the flow of CO$_2$ and measured the transient behavior of Ni/Al$_2$O$_3$-4.6, Ni/Al$_2$O$_3$-6.6, Ni/Al$_2$O$_3$-7.4, and Ni/Al$_2$O$_3$-8.4 catalysts (Fig. 4 and Fig. S7). We observe that CO species quickly disappeared from the surface of the Ni/Al$_2$O$_3$-6.6, Ni/Al$_2$O$_3$-7.4 and Ni/Al$_2$O$_3$-8.4 catalysts. As no CO species were present on the Ni/Al$_2$O$_3$-4.6 catalyst during CO$_2$ methanation, no change in the carbonyl region was observed. In contrast, however, formate species remain on the Ni/Al$_2$O$_3$-4.6, Ni/Al$_2$O$_3$-6.6, Ni/Al$_2$O$_3$-7.4, and Ni/Al$_2$O$_3$-8.4 catalysts. To evaluate whether these formate species are spectator or reactive species, we calculated the peak areas of the adsorbed formate species after stopping CO$_2$ for 1 h. on Ni/Al$_2$O$_3$-4.6 (the catalyst with the lowest TOF) and Ni/Al$_2$O$_3$-8.4 (the catalyst with the highest TOF) as shown in Fig. 5b. The formate peak areas gradually decreased over time. The decrease in peak area was much slower than the measured TOF which suggests this decrease in formate peak area is due to slow desorption rather than reaction and that formate is a spectator species. The decrease in formate peak area may also suggest the slow reaction of formate to methane.

To determine whether the formate species originate from direct CO$_2$ hydrogenation or *via* a CO intermediate, we conducted *in situ* CO hydrogenation FTIR experiments (Fig. 6) and CO hydrogenation reactivity measurements (Fig. S8) on two catalysts: Ni/Al$_2$O$_3$-4.6 and Ni/Al$_2$O$_3$-8.4. These catalysts represent the lowest and highest measured TOF for CO$_2$ methanation and therefore we expect them to show different behavior

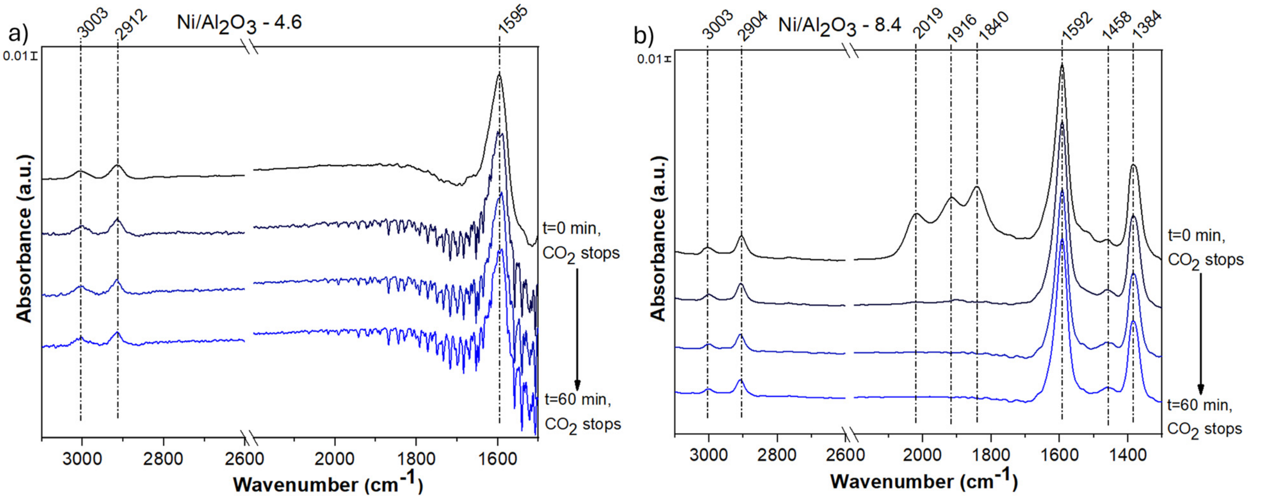

Fig. 4 Transient DRIFTS spectra for (a) Ni/Al$_2$O$_3$-4.6 and (b) Ni/Al$_2$O$_3$-8.4 catalysts; catalysts were exposed to reaction conditions (CO$_2$: H$_2$: Ar = 1 : 4 : 5, 300 °C) for 10 hours, then CO$_2$ was stopped and dynamic changes to the adsorbed species were measured under H$_2$:Ar flow. The black spectrum indicates steady state reaction conditions and blue indicates the catalyst after 1 hour without CO$_2$.

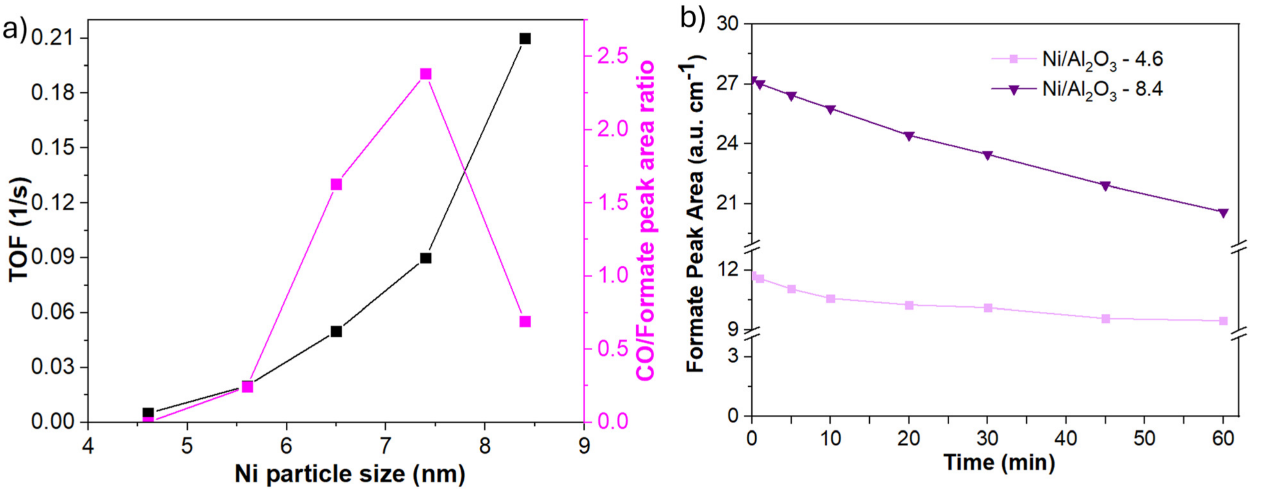

Fig. 5 (a) TOF *vs.* Ni particle size (black) and the ratio of CO : formate peak areas *vs.* Ni particle size from the steady state *in situ* FTIR spectra (pink) and (b) formate IR peak area as a function of time after stopping CO_2. Integrated peak areas are shown in Table S6c.

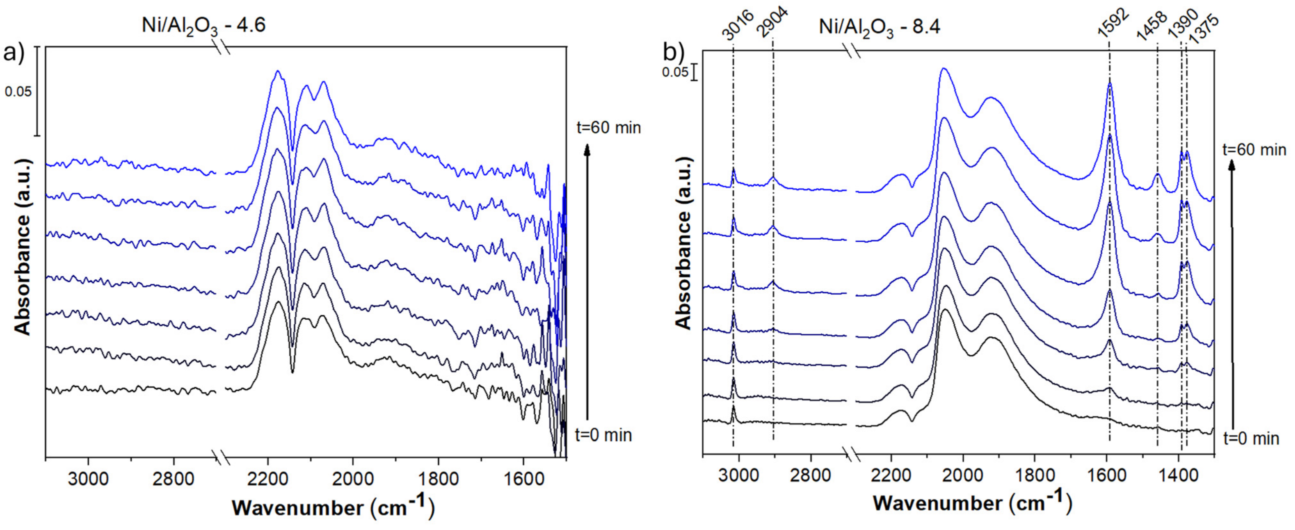

Fig. 6 *In situ* FTIR spectra under CO hydrogenation reaction conditions on (a) Ni/Al_2O_3-4.6 and (b) Ni/Al_2O_3-8.4. The catalysts were reduced *in situ* at 477 °C for 2 h prior to switching to the CO, H_2, Ar (7 : 31 : 62) mixture at 300 °C. The spectra shown were collected across the first hour of reaction; the bottom spectra (black) represents t = 0 min and the top spectra (blue) represents t = 60 min. For all spectra, a background of the reduced catalyst under H_2/Ar flow is subtracted.

under CO hydrogenation conditions. For Ni/Al_2O_3-8.4, under CO methanation conditions, distinct bands corresponding to formate species (1375, 1390, 1592, and 2904 cm^{-1}), bicarbonate species (1458 cm^{-1}), and adsorbed methane (3016 cm^{-1}) were observed and the CO methanation TOF was about 0.13 s^{-1}.[54,70] This TOF on Ni/Al_2O_3-8.4 was lower than the CO_2 methanation TOF (0.21 s^{-1}). In contrast, Ni/Al_2O_3-4.6 showed no detectable formate peaks under CO methanation conditions and the CO methanation TOF was about 0.006 s^{-1} with deactivation over time. This TOF on Ni/Al_2O_3-4.6 was slightly higher than the CO_2 methanation TOF (0.005 s^{-1}). These results suggest that under CO_2 methanation conditions on smaller Ni particles, formate is likely formed directly from CO_2 dissociation but CO methanation proceeds with direct CO cleavage which forms C. This direct CO dissociation and subsequent C accumulation would rationalize the observed deactivation.[71–74] In contrast, the higher TOF for CO_2 methanation than CO methanation on larger Ni particles suggests that the formate pathway can proceed from either CO or CO_2 hydrogenation.

Several groups have proposed that on Ni/Al_2O_3 catalysts, methane formation primarily occurs through formate species adsorbed on the Al_2O_3 surface.[53,75,76] Conversely, Schreiter *et al.* reported that while hydrogen carbonate and carbonate species participate in methane formation, surface formate and carboxylate species may act as spectators.[60] Pan *et al.* proposed that monodentate formate species are more readily hydrogenated than bidentate formate species derived from hydrogen carbonate.[77] Our transient *in situ* FTIR results similarly suggest that the formate species are a spectator species for CO_2 methanation on alumina supported Ni catalysts. We note, however, that we did not observe carbonate and carboxylate species on our catalysts as has been previously suggested by some studies.[60,78] We also observed that CO is likely a reactive species, particularly for larger nickel particles, as has been suggested in the literature.[55,56] Formyl species were also observed on the catalyst with the largest nickel particles. We attribute the presence of these species to the increasing CO_2 methanation performance with particle size. Overall, we suggest that for Ni/Al_2O_3 catalysts, CO_2 methanation proceeds primarily *via* the formate pathway on smaller Ni particles, where the formate species originate from direct CO_2 hydrogenation. As the Ni particle size increases, CO formation becomes more pronounced, and formate species are generated through both CO_2 and CO hydrogenation routes. For the largest Ni particles, formyl and bicarbonate species also appear with CO and formate species. Based on this discussion, a schematic representation of the CO_2 methanation mechanism over Al_2O_3-supported Ni catalysts with varying Ni nanoparticle sizes is provided in Fig. 7.

Beyond reaction mechanism analysis, we examined the interaction of CO_2 with the catalysts to assess its role both as a reactant and as a probe of surface basicity. CO_2 temperature-programmed desorption (CO_2-TPD) was conducted to evaluate the strength of basic adsorption sites, as shown in Fig. 8. Two desorption regions were identified: ≤450 °C, attributed to weak and medium basic sites, and >450 °C, associated with strong basic sites.[79] Previous studies have highlighted the importance of weak and medium basic sites in facilitating CO_2 methanation.[9] The distribution of basic sites, based on integrated peak areas, is summarized in Fig. S9 and Table S7, and correlations between basicity, catalytic activity, and Ni particle size are presented in Fig. 9.

As shown in Fig. 9a, we observe that the percentage of weak + medium basic sites does not follow a specific trend with respect to TOF and Ni particle size. As shown in Fig. 9b, the total basic sites show a downward ‘V’ trend with Ni particle size. Overall, these small changes in basicity do not explain the behavior of TOF as a function of Ni particle size. Basicity is generally suggested to be important for CO_2 methanation,[9] however our measurements indicate a low basic site density that does not change much across the studied set of catalysts (Fig. 9b). In our previous work, we examined the influence of Ni particle size on TiO_2 and CeO_2 supports for CO_2 methanation.[27] The CO_2 desorption profiles obtained from TPD (integrated raw area between 100–900 °C) for Ni/TiO_2 and Ni/CeO_2 catalysts fell within the same range as those observed for Ni/Al_2O_3 in the present study. Thus, despite changing the supports, the CO_2 desorption behavior remained comparable, particularly for Ni/TiO_2 and Ni/Al_2O_3. The CO_2 desorption can be attributed to catalyst basicity, leading us to conclude that Ni particle size exerts minimal influence on the basicity of Al_2O_3-supported catalysts.

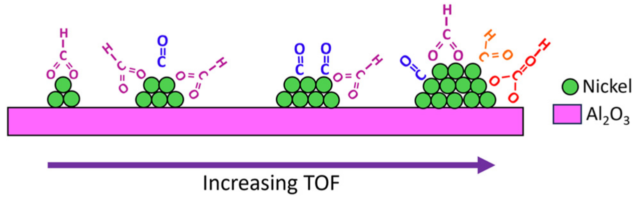

Fig. 7 Proposed surface species and reactivity trend of the catalysts studied in this work.

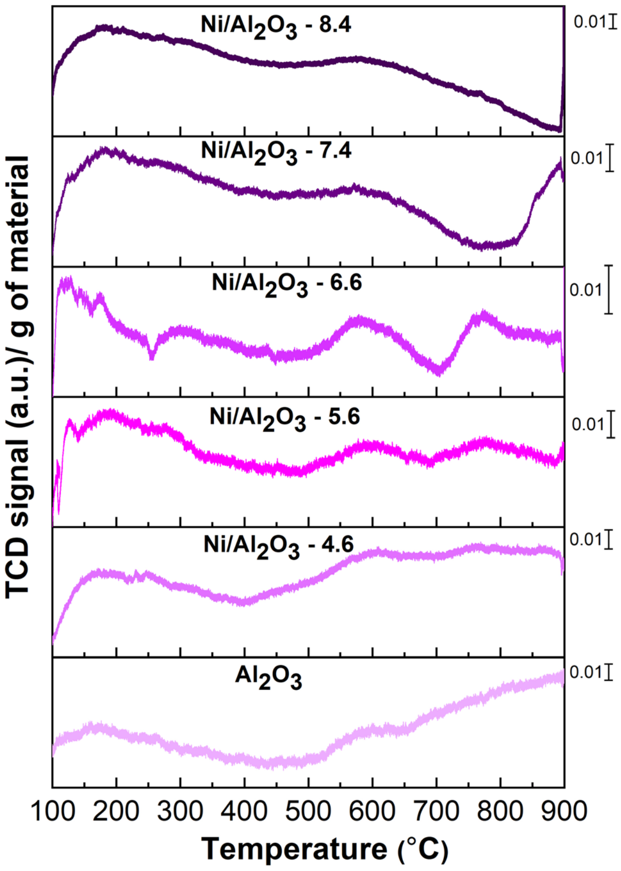

Fig. 8 CO_2 TPD on Ni/Al_2O_3 catalysts studied in this work.

Since methanation takes place in the presence of H_2 (a reducing agent) and CO_2 (an oxidizing agent), the reduction and oxidation behavior of the Ni catalysts is important to understand activity trends. H_2 TPR and O_2 TPO profiles of the series of Ni-based catalysts are shown in Fig. 10. Both experiments were conducted on fresh, reduced and passivated catalysts where we expect some variation in the ratio of metallic to oxidized Ni between catalysts, therefore we analyze the results qualitatively rather than quantitatively. As shown in Fig. 10a, the observed peak below 400 °C may represent the reduction of NiO species to Ni^0. The much smaller peaks above 400 °C represent the reduction of a nickel aluminate phase, which is observed by XRD (Fig. S1).[80,81] Similarly in Fig. 10b, the observed peaks

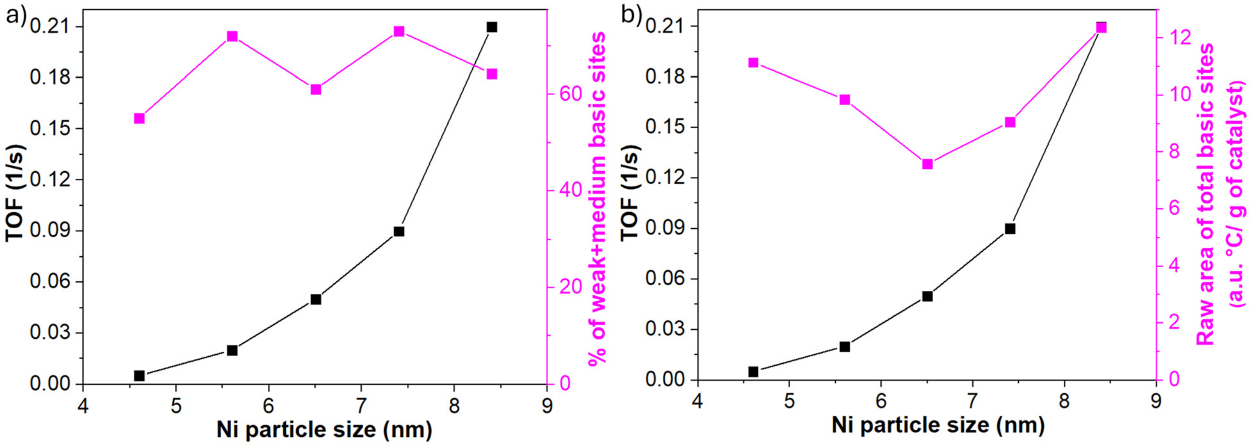

Fig. 9 The CO_2 methanation turnover frequency (black) and (a) % of weak + medium basic sites (magenta) or (b) the area of total basic sites (desorption from 100–900 °C) (magenta) from temperature programmed desorption as a function of Ni particle size.

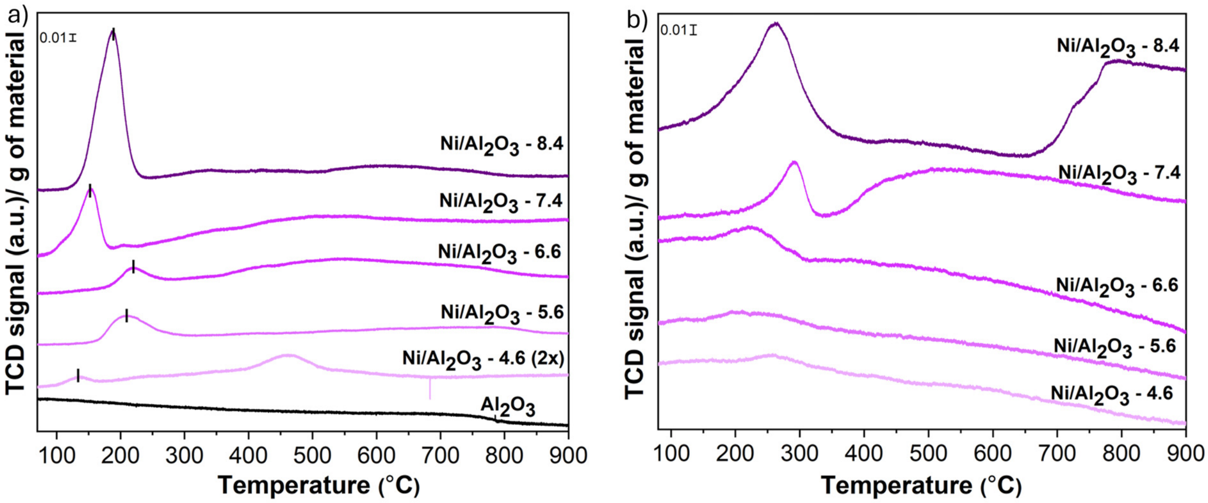

Fig. 10 (a) H_2 TPR and (b) O_2 TPO on Ni/Al_2O_3 catalysts. It should be noted that after synthesis the catalysts were reduced at 477 °C for 12 hours in H_2 and then passivated for 30 minutes and stored in air prior to the TPR and TPO.

below 500 °C represent the oxidation of Ni^0 to NiO.[82–84] These results indicate that Ni is able to be both oxidized and reduced at the reaction temperature of 300 °C. While we observe intensity changes across the set of catalysts, likely due to metal content, the overall redox behavior remains similar.

We also performed *ex situ* XPS to assess the catalyst electronic structure for fresh and spent Ni/Al_2O_3-4.6 and Ni/Al_2O_3-8.4 catalysts as presented in Fig. 11. Fig. 11 shows the deconvoluted Ni 2p spectra of Ni/Al_2O_3-4.6 and Ni/Al_2O_3-8.4 before (a, c) and after (b,d) the reaction. The Ni^{2+} $2p_{3/2}$ peak was observed at 855.20 eV for both fresh and spent catalysts.[85,86] The Ni^0 phase appeared to be absent on the fresh sample but was ~7.5 atomic % of the Ni on the spent catalyst for both Ni/Al_2O_3-4.6 and Ni/Al_2O_3-8.4. This change in species before and after reaction suggests some degree of redox activity under reaction conditions, in agreement with the TPR and TPO results. Both catalysts showed $NiAl_2O_4$ spinel peaks which are characteristic of Ni/Al_2O_3 catalysts. As the XPS measurements were conducted *ex situ* after air exposure, the observed predominantly Ni oxide species are expected. Because XPS is surface-sensitive (probing depth ~5 nm), metallic Ni species may exist beneath a Ni oxide layer and be undetected by this technique, depending on particle size, resulting in signals corresponding mainly to Ni^{2+} rather than Ni^0 for the fresh catalysts. In contrast, TPO captures oxidation of all reducible Ni species, including subsurface metal, and thus may exhibit a Ni-metal oxidation feature even when the surface is oxidized. Interestingly, a small amount of Ni^0 was detected in the spent catalysts by XPS, suggesting that reduction (and likely oxidation) occurs under reaction conditions. *In situ* techniques to directly probe this behavior, such as *in situ* XPS or XAS, however, are outside the scope of this study.

From previous reports in the literature, metallic Ni sites are known to facilitate H_2 dissociation and CO_2

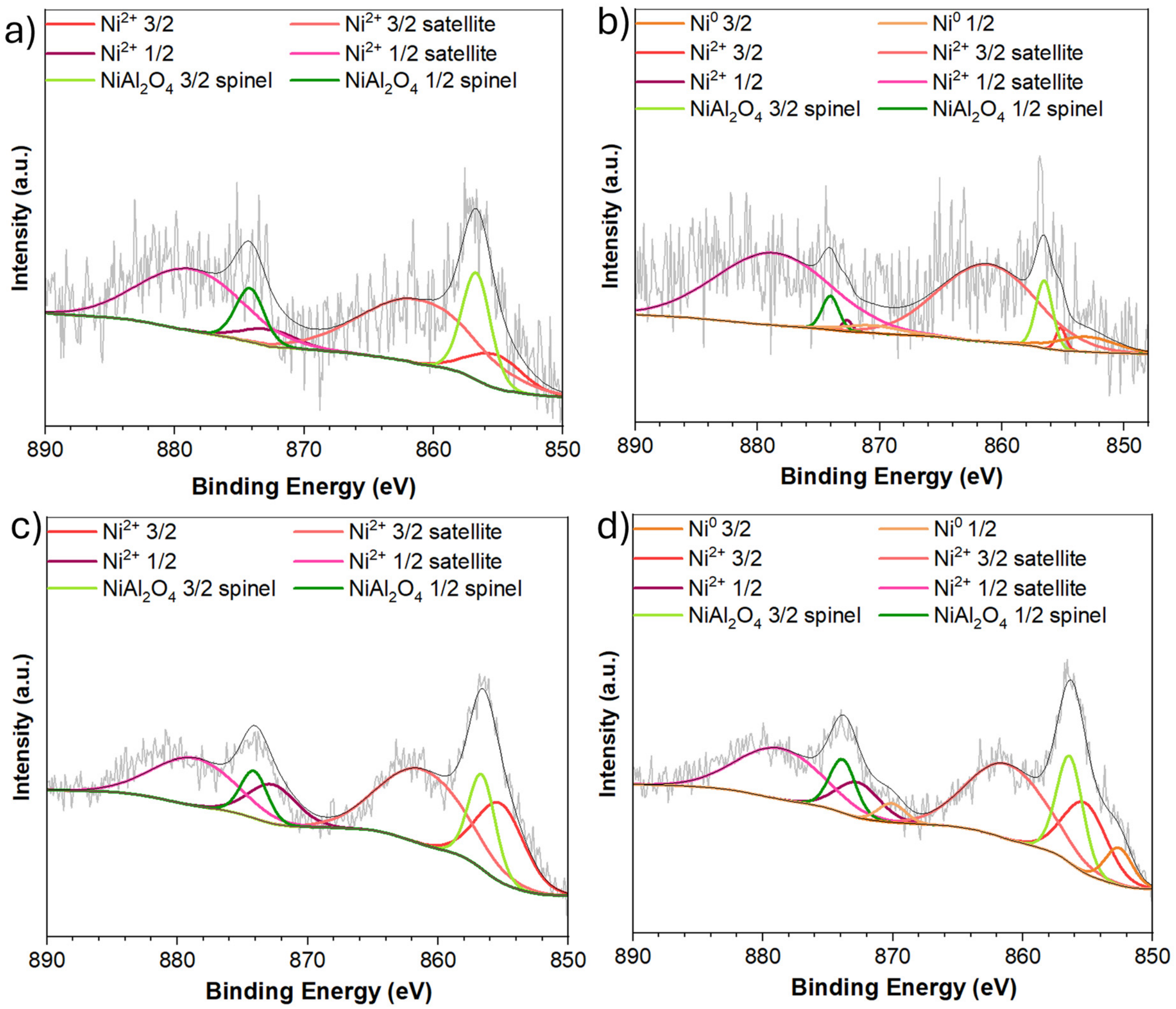

Fig. 11 Deconvoluted Ni 2p XPS spectra of (a) fresh Ni/Al_2O_3-4.6, (b) spent Ni/Al_2O_3-4.6, (c) fresh Ni/Al_2O_3-8.4, and (d) spent Ni/Al_2O_3-8.4.

hydrogenation,[53,87] while adjacent NiO domains can promote CO_2 adsorption and activation.[88,89] Bi *et al.* studied MCM-41 supported nickel catalysts where they found that the co-existence of metallic Ni and NiO species at a sufficient molar ratio creates a metal Ni–NiO interface, which facilitates the activation of reactants and improves CO_2 methanation performance.[90] As reported in previous studies, CO species are adsorbed on metallic Ni sites,[61,62] whereas formate species tend to adsorb and stabilize on NiO sites rather than on metallic Ni.[63,64] Though we cannot directly correlate the oxidation and reduction behavior with metallic Ni and NiO respectively, we suggest that a balance between the reducing and oxidizing characteristics of the catalysts may synergistically enhance the methanation reaction performance.

Conclusion

We have observed a positive relationship between Ni particle size and TOF for CO_2 methanation. We suggest that across all Ni/Al_2O_3 catalysts studied in this work, methanation occurs *via* a formate pathway. On the most active catalysts with larger Ni particles, CO_2 methanation follows a parallel CO + formate pathway. The highest reaction rate is observed when bicarbonate and short-lived formyl species are present in addition to CO and formate. The catalysts' reduction and oxidation behavior are thought to work synergistically to improve CO_2 methanation performance. Catalyst basicity, however, does not have a direct correlation with methanation activity trends observed on the set of Ni/Al_2O_3 catalysts.

Conflicts of interest

We declare no conflicts of interest.

Data availability

Reproduction data for all figures is provided at: https://doi.org/10.7910/DVN/FS9AGD.

Supplementary information (SI): XRD, calculations verifying the absence of transport limitations, FTIR spectra of adsorbed CO, additional reactivity data, and FTIR peak assignments and peak areas, and areas used to quantify basic sites are available in the supplementary information. See DOI: https://doi.org/10.1039/d5nr03101j.

Acknowledgements

We acknowledge the use of the WVU Shared Research Facilities for XRD, TEM analysis, and the WVU Energy Institute Analytical Lab for ICP analysis. The STEM portion of this research was supported by the Center for Nanophase Materials Sciences (CNMS), which is a US Department of Energy, Office of Science User Facility at Oak Ridge National Laboratory. The authors acknowledge the financial support from West Virginia Higher Education Policy Commission (WV HEPC) Research Challenge Grant RCG23-009: Metal-Embedded Carbon-based Catalytic Membranes for Co-production of Ammonia and Ethylene. For XPS analysis, the authors also acknowledge the financial support of the University of Michigan College of Engineering, and technical support from the Michigan Center for Materials Characterization.

References

1 E. S. Sanz-Pérez, C. R. Murdock, S. A. Didas and C. W. Jones, *Chem. Rev.*, 2016, **116**, 11840–11876.

2 P. Styring, S. McCord and S. Rackley, in *Negative Emissions Technologies for Climate Change Mitigation*, Elsevier, 2023, pp. 391–413.

3 L. Fu, Z. Ren, W. Si, Q. Ma, W. Huang, K. Liao, Z. Huang, Y. Wang, J. Li and P. Xu, *J. CO_2 Util.*, 2022, **66**, 102260.

4 J. Ashok, S. Pati, P. Hongmanorom, Z. Tianxi, C. Junmei and S. Kawi, *Catal. Today*, 2020, **356**, 471–489.

5 L. Karam, M. C. Bacariza, J. M. Lopes, C. Henriques, J. Reboul, N. E. Hassan and P. Massiani, *J. CO_2 Util.*, 2021, **51**, 101651.

6 C. Lv, L. Xu, M. Chen, Y. Cui, X. Wen, Y. Li, C. Wu, B. Yang, Z. Miao, X. Hu and Q. Shou, *Front. Chem.*, 2020, **8**, 269.

7 O. E. Medina, A. A. Amell, D. López and A. Santamaría, *Renewable Sustainable Energy Rev.*, 2025, **207**, 114926.

8 A. Quindimil, U. De-La-Torre, B. Pereda-Ayo, A. Davó-Quiñonero, E. Bailón-García, D. Lozano-Castelló, J. A. González-Marcos, A. Bueno-López and J. R. González-Velasco, *Catal. Today*, 2020, **356**, 419–432.

9 L. Shen, J. Xu, M. Zhu and Y. F. Han, *ACS Catal.*, 2020, **10**, 14581–14591.

10 C. Vogt, E. Groeneveld, G. Kamsma, M. Nachtegaal, L. Lu, C. J. Kiely, P. H. Berben, F. Meirer and B. M. Weckhuysen, *Nat. Catal.*, 2018, **1**, 127–134.

11 S. Kuhaudomlap, A. Srifa, W. Koo-Amornpattana, C. Fukuhara and S. Ratchahat, *Sci. Rep.*, 2024, **14**, 23149.

12 S. Lyu, D. Zhao, H. Zhang, H. Li, F. Wen, Q. Zhou, R. Zhang, Y. Wu, C. Hou, G. Xia, R. Xu and X. Li, *Carbon Capture Sci. Technol.*, 2025, **14**, 100381.

13 C. Italiano, J. Llorca, L. Pino, M. Ferraro, V. Antonucci and A. Vita, *Appl. Catal., B*, 2020, **264**, 118494.

14 N. A. Ayub, H. Bahruji and A. H. Mahadi, *RSC Adv.*, 2021, **11**, 31807–31816.

15 M. A. Abir and M. R. Ball, *Chem Catal.*, 2023, **3**, 100852.

16 C. Vogt, M. Monai, E. B. Sterk, J. Palle, A. E. M. Melcherts, B. Zijlstra, E. Groeneveld, P. H. Berben, J. M. Boereboom, E. J. M. Hensen, F. Meirer, I. A. W. Filot and B. M. Weckhuysen, *Nat. Commun.*, 2019, **10**, 5330.

17 J. F. M. Simons, T. J. De Heer, R. C. J. Van De Poll, V. Muravev, N. Kosinov and E. J. M. Hensen, *J. Am. Chem. Soc.*, 2023, **145**, 20289–20301.

18 K. Wang, Y. Men, S. Liu, J. Wang, Y. Li, Y. Tang, Z. Li, W. An, X. Pan and L. Li, *Fuel*, 2021, **304**, 121388.

19 E. B. Sterk, A.-E. Nieuwelink, M. Monai, J. N. Louwen, E. T. C. Vogt, I. A. W. Filot and B. M. Weckhuysen, *JACS Au*, 2022, **2**, 2714–2730.

20 G. Spanò, M. Ferri, R. Cheula, M. Monai, B. M. Weckhuysen and M. Maestri, *ACS Catal.*, 2025, **15**, 8194–8203.

21 S. He, C. Li, H. Chen, D. Su, B. Zhang, X. Cao, B. Wang, M. Wei, D. G. Evans and X. Duan, *Chem. Mater.*, 2013, **25**, 1040–1046.

22 S. Ratchahat, M. Sudoh, Y. Suzuki, W. Kawasaki, R. Watanabe and C. Fukuhara, *J. CO_2 Util.*, 2018, **24**, 210–219.

23 R. Zhou, N. Rui, Z. Fan and C. Liu, *Int. J. Hydrogen Energy*, 2016, **41**, 22017–22025.

24 Y. Yan, Y. Dai, Y. Yang and A. A. Lapkin, *Appl. Catal., B*, 2018, **237**, 504–512.

25 L. Lin, C. A. Gerlak, C. Liu, J. Llorca, S. Yao, N. Rui, F. Zhang, Z. Liu, S. Zhang, K. Deng, C. B. Murray, J. A. Rodriguez and S. D. Senanayake, *J. Energy Chem.*, 2021, **61**, 602–611.

26 D. Adhikari, C. A. Whitcomb, W. Zhang, S. Zhang and R. J. Davis, *J. Catal.*, 2024, **438**, 115708.

27 M. A. Abir, R. E. Phillips, J. Z. M. Harrah and M. R. Ball, *Catal. Sci. Technol.*, 2024, **14**, 4506–4521.

28 D. Méndez-Mateos, V. L. Barrio, J. M. Requies and M. Gil-Calvo, *Environ. Sci. Pollut. Res.*, 2023, **31**, 36093–36117.

29 A. Quindimil, U. De-La-Torre, B. Pereda-Ayo, A. Davó-Quiñonero, E. Bailón-García, D. Lozano-Castelló, J. A. González-Marcos, A. Bueno-López and J. R. González-Velasco, *Catal. Today*, 2020, **356**, 419–432.

30 Z. Shang, S. Li, L. Li, G. Liu and X. Liang, *Appl. Catal., B*, 2017, **201**, 302–309.

31 J. Yu, B. Feng, S. Liu, X. Mu, E. Lester and T. Wu, *Appl. Energy*, 2022, **315**, 119036.

32 P. Riani, E. Spennati, M. V. Garcia, V. S. Escribano, G. Busca and G. Garbarino, *Int. J. Hydrogen Energy*, 2023, **48**, 24976–24995.

33 W. Gac, W. Zawadzki, M. Rotko, G. Słowik and M. Greluk, *Top. Catal.*, 2019, **62**, 524–534.

34 W. Gac, W. Zawadzki, M. Rotko, M. Greluk, G. Słowik and G. Kolb, *Catal. Today*, 2020, **357**, 468–482.

35 C. Liang, H. Tian, G. Gao, S. Zhang, Q. Liu, D. Dong and X. Hu, *Int. J. Hydrogen Energy*, 2020, **45**, 531–543.

36 G. Garbarino, C. Wang, T. Cavattoni, E. Finocchio, P. Riani, M. Flytzani-Stephanopoulos and G. Busca, *Appl. Catal., B*, 2019, **248**, 286–297.

37 Z. Zhang, Y. Tian, L. Zhang, S. Hu, J. Xiang, Y. Wang, L. Xu, Q. Liu, S. Zhang and X. Hu, *Int. J. Hydrogen Energy*, 2019, **44**, 9291–9306.

38 A. Karelovic and P. Ruiz, *Appl. Catal., B*, 2012, **113–114**, 237–249.

39 F. Wang, K. Han, L. Xu, H. Yu and W. Shi, *Industrial and Engineering Chemistry Research*, 2021, **60**, 3324–3333.

40 A. Wong, Q. Liu, S. Griffin, A. Nicholls and J. R. Regalbuto, *Science*, 2017, **358**, 1427–1430.

41 L. Jiao and J. R. Regalbuto, *J. Catal.*, 2008, **260**, 329–341.

42 G. D. Weatherbee and C. H. Bartholomew, *J. Catal.*, 1981, **68**, 67–76.

43 *Synthesis of Solid Catalysts*, ed. K. P. De Jong, Wiley, 1st edn, 2009.

44 W. L. Vrijburg, J. W. A. Van Helden, A. J. F. Van Hoof, H. Friedrich, E. Groeneveld, E. A. Pidko and E. J. M. Hensen, *Catal. Sci. Technol.*, 2019, **9**, 2578–2591.

45 N. Fairley, V. Fernandez, M. Richard-Plouet, C. Guillot-Deudon, J. Walton, E. Smith, D. Flahaut, M. Greiner, M. Biesinger, S. Tougaard, D. Morgan and J. Baltrusaitis, *Appl. Surf. Sci. Adv.*, 2021, **5**, 100112.

46 K. Hadjiivanov, H. Knözinger and M. Mihaylov, *J. Phys. Chem. B*, 2002, **106**, 2618–2624.

47 F. C. Meunier, *Catal. Sci. Technol.*, 2022, **12**, 7433–7438.

48 C.-D. Tan and J. F. Ni, *J. Chem. Eng. Data*, 1997, **42**, 342–345.

49 A. J. McCue, G. A. Mutch, A. I. McNab, S. Campbell and J. A. Anderson, *Catal. Today*, 2016, **259**, 19–26.

50 M. A. Vannice and S. Y. Wang, *J. Phys. Chem.*, 1981, **85**, 2543–2546.

51 K. S. W. Singh, J. Rouquerol, G. Bergeret, P. Gallezot, M. Vaarkamp, D. C. Koningsberger, A. K. Datye, J. W. Niemantsverdriet, T. Butz, G. Engelhardt, G. Mestl, H. Knözinger and H. Jobic, in *Handbook of Heterogeneous Catalysis*, ed. G. Ertl, H. Knözinger and J. Weitkamp, Wiley, 1st edn, 1997, pp. 427–582.

52 Z. Zhang, Y. Tian, L. Zhang, S. Hu, J. Xiang, Y. Wang, L. Xu, Q. Liu, S. Zhang and X. Hu, *Int. J. Hydrogen Energy*, 2019, **44**, 9291–9306.

53 A. Cárdenas-Arenas, A. Quindimil, A. Davó-Quiñonero, E. Bailón-García, D. Lozano-Castelló, U. De-La-Torre, B. Pereda-Ayo, J. A. González-Marcos, J. R. González-Velasco and A. Bueno-López, *Appl. Catal., B*, 2020, **265**, 118538.

54 C. Schild, A. Wokaun, R. A. Koeppel and A. Baiker, *J. Phys. Chem.*, 1991, **95**, 6341–6346.

55 M. Kock, E. Kowalewski, D. Iltsiou, J. Mielby and S. Kegnæs, *ChemCatChem*, 2024, **16**(4), DOI: 10.1002/cctc.202301447.

56 J. Y. Lim, J. McGregor, A. J. Sederman and J. S. Dennis, *Chem. Eng. Sci.*, 2016, **141**, 28–45.

57 Q. Pan, J. Peng, T. Sun, S. Wang and S. Wang, *Catal. Commun.*, 2014, **45**, 74–78.

58 M. Hasan, T. Asakoshi, H. Muroyama, T. Matsui and K. Eguchi, *Phys. Chem. Chem. Phys.*, 2021, **23**, 5551–5558.

59 A. Quindimil, J. A. Onrubia-Calvo, A. Davó-Quiñonero, A. Bermejo-López, E. Bailón-García, B. Pereda-Ayo, D. Lozano-Castelló, J. A. González-Marcos, A. Bueno-López and J. R. González-Velasco, *J. CO_2 Util.*, 2022, **57**, 101888.

60 N. Schreiter, J. Kirchner and S. Kureti, *Catal. Commun.*, 2020, **140**, 105988.

61 Y. Yamauchi, Y. Hoshimoto, T. Kawakita, T. Kinoshita, Y. Uetake, H. Sakurai and S. Ogoshi, *J. Am. Chem. Soc.*, 2022, **144**, 8818–8826.

62 Y. T. Wong and R. Hoffmann, *J. Phys. Chem.*, 1991, **95**, 859–867.

63 R. A. El-Salamony, K. Acharya, A. S. Al-Fatesh, A. I. Osman, S. B. Alreshaidan, N. S. Kumar, H. Ahmed and R. Kumar, *Mol. Catal.*, 2023, **547**, 113378.

64 H. S. Chitturi, Y. Lavanya, Y. Varun, A. Ramesh, S. H. Pamu, I. Sreedhar and S. A. Singh, *J. Mater. Chem. A*, 2025, **13**, 7422–7444.

65 D. Heyl, U. Rodemerck and U. Bentrup, *ACS Catal.*, 2016, **6**, 6275–6284.

66 J. Zhu, Y. Su, J. Chai, V. Muravev, N. Kosinov and E. J. M. Hensen, *ACS Catal.*, 2020, **10**, 11532–11544.

67 D. A. Jurado A., M. D. Higham, Y. R. Poh, C. R. A. Catlow and I. Krossing, *J. Catal.*, 2025, **446**, 115997.

68 R. Guil-López, N. Mota, J. Llorente, E. Millán, B. Pawelec, J. L. G. Fierro and R. M. Navarro, *Materials*, 2019, **12**, 3902.

69 D. Rivero-Mendoza, J. Stanley, J. Scott and K.-F. Aguey-Zinsou, *Catalysts*, 2016, **6**, 170.

70 H. Xiao, J. Dong, Y. Zhang, X. Cao, Y. Li, D. He, Y. Luo, P. Wang and H. Wang, *RSC Adv.*, 2024, **14**, 39061–39068.

71 F. Mateus, P. Teixeira, J. M. Lopes, C. Henriques and C. Bacariza, *Energy Fuels*, 2023, **37**, 8552–8562.

72 Z. Guo, S. Chen and B. Yang, *iScience*, 2023, **26**, 106237.

73 S. Ozdogan, *J. Catal.*, 1983, **83**, 257–266.

74 J. Engbæk, O. Lytken, J. H. Nielsen and I. Chorkendorff, *Surf. Sci.*, 2008, **602**, 733–743.

75 N. A. A. Fatah, A. A. Jalil, N. F. M. Salleh, M. Y. S. Hamid, Z. H. Hassan and M. G. M. Nawawi, *Int. J. Hydrogen Energy*, 2020, **45**, 18562–18573.

76 Q. Pan, J. Peng, T. Sun, S. Wang and S. Wang, *Catal. Commun.*, 2014, **45**, 74–78.

77 Q. Pan, J. Peng, T. Sun, S. Wang and S. Wang, *Catal. Commun.*, 2014, **45**, 74–78.

78 A. A. Alkhoori, O. Elmutasim, A. A. Dabbawala, M. A. Vasiliades, K. C. Petallidou, A.-H. Emwas, D. H. Anjum, N. Singh, M. A. Baker, N. D. Charisiou, M. A. Goula, A. M. Efstathiou and K. Polychronopoulou, *ACS Appl. Energy Mater.*, 2023, **6**, 8550–8571.

79 C. Sun, P. Beaunier, V. La Parola, L. F. Liotta and P. Da Costa, *ACS Appl. Nano Mater.*, 2020, **3**, 12355–12368.

80 Z. Yaakob, A. Bshish, A. Ebshish, S. Tasirin and F. Alhasan, *Materials*, 2013, **6**, 2229–2239.

81 M. Cai, J. Wen, W. Chu, X. Cheng and Z. Li, *J. Nat. Gas Chem.*, 2011, **20**, 318–324.

82 Y. Unutulmazsoy, R. Merkle, D. Fischer, J. Mannhart and J. Maier, *Phys. Chem. Chem. Phys.*, 2017, **19**, 9045–9052.

83 B. A. Abd-El-Nabey, S. El-Housseiny, A. M. Abdel-Gaber and M. E. Mohamed, *Results Chem.*, 2023, **5**, 100876.

84 A. Larsson, S. Gericke, A. Grespi, V. Koller, J. Eidhagen, X. Yue, E. Frampton, S. Appelfeller, A. Generalov, A. Preobrajenski, J. Pan, H. Over and E. Lundgren, *npj Mater. Degrad.*, 2024, **8**, 39.

85 A. Quindimil, U. De-La-Torre, B. Pereda-Ayo, A. Davó-Quiñonero, E. Bailón-García, D. Lozano-Castelló, J. A. González-Marcos, A. Bueno-López and J. R. González-Velasco, *Catal. Today*, 2020, **356**, 419–432.

86 O. Netskina, S. Mucha, J. Veselovskaya, V. Bolotov, O. Komova, A. Ishchenko, O. Bulavchenko, I. Prosvirin, A. Pochtar and V. Rogov, *Materials*, 2021, **14**, 6789.

87 H. Wang, Z. Li, G. Cui and M. Wei, *ACS Appl. Mater. Interfaces*, 2023, **15**, 19021–19031.

88 Z. Zhang, K. Feng and B. Yan, *Catal. Sci. Technol.*, 2022, **12**, 4698–4708.

89 J. Zhu, F. Cannizzaro, L. Liu, H. Zhang, N. Kosinov, I. A. W. Filot, J. Rabeah, A. Brückner and E. J. M. Hensen, *ACS Catal.*, 2021, **11**, 11371–11384.

90 Q. Bi, X. Huang, G. Yin, T. Chen, X. Du, J. Cai, J. Xu, Z. Liu, Y. Han and F. Huang, *ChemCatChem*, 2019, **11**, 1295–1302.